

# Patherea: Cell Detection and Classification for the 2020s

Dejan Štepec<sup>a</sup>, Maja Jerše<sup>b</sup>, Snežana Đokić<sup>c</sup>, Jera Jeruc<sup>b</sup>, Nina Zidar<sup>b</sup>, Danijel Skočaj<sup>a</sup>

<sup>a</sup>*Faculty of Computer and Information Science, University of Ljubljana, Večna pot 113, 1000 Ljubljana, Slovenia*

<sup>b</sup>*Institute of Pathology, Faculty of Medicine, University of Ljubljana, Korytkova 2, 1000 Ljubljana, Slovenia*

<sup>c</sup>*Institute of Oncology Ljubljana, Zaloška cesta 2, 1000 Ljubljana, Slovenia*

---

## Abstract

This paper presents a Patherea, a framework for point-based cell detection and classification that provides a complete solution for developing and evaluating state-of-the-art approaches. We introduce a large-scale dataset collected to directly replicate a clinical workflow for Ki-67 proliferation index estimation and use it to develop an efficient point-based approach that directly predicts point-based predictions, without the need for intermediate representations. The proposed approach effectively utilizes point proposal candidates with the hybrid Hungarian matching strategy and a flexible architecture that enables the usage of various backbones and (pre)training strategies. We report state-of-the-art results on existing public datasets - Lizard, BRCA-M2C, BCDData, and the newly proposed Patherea dataset. We show that the performance on existing public datasets is saturated and that the newly proposed Patherea dataset represents a significantly harder challenge for the recently proposed approaches. We also demonstrate the effectiveness of recently proposed pathology foundational models that our proposed approach can natively utilize and benefit from. We also revisit the evaluation protocol that is used in the broader field of cell detection and classification and identify the erroneous calculation of performance metrics. Patherea provides a benchmarking utility that addresses the identified issues and enables a fair comparison of different approaches. The dataset and the code will be publicly released upon acceptance.

**Keywords:** Pathology, Ki-67, detection, classification, vision transformer

---

\*Corresponding author. Email: dejan.stepec@patherea.ai

## 1. Introduction

The emergence of whole-slide scanners has enabled the scanning of a complete microscopic tissue slide and the creation of a single high-resolution digital file - a gigapixel whole slide image (WSI). The so-called digital pathology represents recent digitalization efforts in the medical field of pathology to omit the need for traditional diagnostics to be performed under the microscope (Mukhopadhyay et al., 2018). However, with the emergence of whole slide scanners and progress in AI and computer vision, it is simultaneously undergoing another big transformation, shifting from digital to computational pathology – the analysis of digitized data using AI (Bera et al., 2019; Cui and Zhang, 2021). Various computer vision approaches have been applied for histopathology analysis and diagnostics with proven comparative performance with the pathologists (Bejnordi et al., 2017; Bulten et al., 2022).

Cancer diagnostics is traditionally performed by pathologists under the microscope, which includes quantifying the immunohistochemical expression of various proteins on specially stained tissue samples. In practice, this means counting hundreds or thousands of cells of a particular class and interest (e.g., positively, and negatively stained tumor cells) which forms a basis to derive prognostic scoring markers (Dowsett et al., 2011). Ki-67 proliferation index represents one of the most widely used prognostic markers in different cancer types (e.g., breast cancer, neuroendocrine tumors, lymphomas, sarcomas) and identifies the proportion of tumor cells in the proliferation phase (i.e., tumor growth rate). Computing such a scoring is a highly time-consuming manual work for a pathologist, however it enables classification and grading of tumors, evaluation of their malignant potential, and is the basis for determining an effective treatment. In practice, less accurate approaches are used Mikami et al. (2013); Polley et al. (2013), which leads to lower interobserver concordance and reproducibility.

Automating cell detection and classification represents a key step for performing diagnostics in a more efficient and reproducible manner and has been one of the first topics to be addressed in histopathology image analysis Xing and Yang (2016). Supervised-learning-based approaches require expertly labeled datasets, which are costly to obtain in sufficient quantities in comparison with natural images in the broader computer vision domain. Most approaches utilize point-based annotations, which are easier to obtain in comparison with bounding boxes or segmentation masks and are most often not needed to support the end application in terms of diagnostics. Various point-based deep-learning-based approaches have been proposed in recent years (Xie et al., 2015, 2018; Lee et al., 2021; Abousamra

et al., 2021; Huang et al., 2023b,a; Pina et al., 2024) that require the use of intermediate representations to regress and classify cell centers, or the use of existing complex DETR-based (Carion et al., 2020) object-detection architectures, specialized to support point annotations. In contrast, we provide a direct point-to-point approach, that utilizes general computer vision backbones (Dosovitskiy et al., 2021; Liu et al., 2022), with simple architecture, fast convergence, and support for the use of existing large-scale pathology pretrained foundational models.

Generating labeled data for different possible diseases is not only prohibitively expensive and time-consuming, but in the medical domain, often impossible due to low occurrence and natural and technical variability present in the samples. On the other hand, diagnostics is performed on a daily basis around the world, with workflows being digitized and unlabeled samples being stored in large quantities. Similar to general language and vision domains (Radford et al., 2019, 2021; He et al., 2022; Oquab et al., 2024), pathology foundational models have been recently presented (Filiot et al., 2023; Chen et al., 2024; Vorontsov et al., 2023; Dippel et al., 2024; Xu et al., 2024; Nechaev et al., 2024) that utilize vast amounts of unlabeled data from up to millions of samples from various diseases, stainings and instruments.

Limited labeled training data is needed to train or fine-tune the models on a specific downstream task of interest, as well as to benchmark different approaches. Publicly available cell detection and classification datasets in pathology are rare and mostly consists of the standard hematoxylin and eosin (H&E) staining and with at most couple of tens of thousands annotated cell centers, often annotated with an semi-automatic approach and in a patch-based manner, which does not reflect the actual pathologists workflow (Sirinukunwattana et al., 2016; Huang et al., 2020; Graham et al., 2021; Abousamra et al., 2021; Ryu et al., 2023). Different metrics and their implementations - some of them flawed, are used, making it difficult to compare different proposed approaches.

To summarize, we make the following contributions:

- We propose a novel end-to-end point-based cell detection and classification architecture based on Vision Transformers that completely removes the need for pre-processing and post-processing, enabling fast convergence and utilization of domain-specific foundational models.
- We identify and address the erroneous calculation of performance metrics in point-based object detection in the domain of pathology and provide a benchmarking framework that addresses the identified issues and enables a fair comparison of different approaches.

- To the best of our knowledge, we present<sup>1</sup> the largest manually labeled point-based Ki-67 dataset that was collected by directly mimicking the clinical practice, utilizing the full-resolution WSIs. We demonstrate that the performance on existing public datasets is saturated and that the newly proposed dataset represents a significantly harder challenge for the recently proposed approaches.
- We evaluate the proposed approaches on existing public and newly proposed cell detection and classification datasets and improve upon recently proposed state-of-the-art approaches - in some cases by a significant margin.
- We make all of our Patherea code (Patherea-P2P, Patherea-FCRN, benchmarking code) publicly available for research use<sup>2</sup>.

## 2. Related Work

### 2.1. Point-based Cell Detection

Cell detection and classification in histopathology is a challenging problem due to variance in cell shape and appearance. This is further exacerbated by overlapping cells, staining artifacts, scanning artifacts, out-of-focus regions, and in general, the sheer amount of cells present in a selected field-of-view. This represents a significant challenge even for trained pathologists when performing diagnostics under the microscope (Mikami et al., 2013; Polley et al., 2013). While limited success can be achieved with conventional image processing approaches, that are included in some of the open-source pathology software’s Bankhead et al. (2017), we limit ourselves to learning-based approaches.

The early approaches were based on classifying small patches centered on the ground-truth cell-center locations of whether the center of the patch belongs to the foreground or background, or by learning a distance function for each pixel in a centered patch (Kainz et al., 2015; Sirinukunwattana et al., 2016). The intermediate representation in the form of different distance-based functions has later evolved by taking into account the neighboring context and a direct regression on full-sized patches (Xie et al., 2018; Huang et al., 2020). MCSpatNet (Abousamra et al., 2021) has recently introduced Ripley’s K-function that represents an expected number of neighbors of a specific type, around the limited vicinity of the

---

<sup>1</sup>TBD

<sup>2</sup>TBD



target cell location. By learning to predict the vectorized form of a K-function, the model essentially learns the spatial representation. These approaches regress to an intermediate representation, which needs to be pre-computed for training the regression model. In inference, the predicted intermediate representation needs to be post-processed (e.g., with non-maxima suppression) to get the individual cell locations and cell types. Such approaches are better-suited for cell-counting, while error-prone in cell localization tasks.

Cell detection and classification represents a similar task to crowd counting and localization (Li et al., 2018; Song et al., 2021) in the broader computer vision domain. P2PNet (Song et al., 2021) represents a purely point-based approach, without the need for intermediate representations. This is achieved by assigning an optimal target to each proposal candidate in a one-to-one fashion using the Hungarian algorithm. A similar approach is utilized in Detection-Transformers (DETRs), which were recently proposed for bounding-box-based object detection (Carion et al., 2020). DETR-based approaches were recently adapted for point-based detection and applied to pathology (Huang et al., 2023b,a). From the implementation perspective, the standard bounding-box DETR is utilized with  $1 \times 1$   $px$  bounding box centered on ground-truth point-based annotations. The naive implementation diminishes the predictive power of visual features near the cell center, prompting the development of various advancements to address this limitation. ACFormer (Huang et al., 2023b) utilizes a DETR-based architecture and proposes an Affine-Consistent-Transformer by using local and global networks to enhance the spatial scale consistency. PGT (Huang et al., 2023a) is also based on DETR and introduces a learnable Grouping Transfer that leverages the similarity between nuclei and their cluster representation to take into account the spatial context, similar to MCSpatNet (Abousamra et al., 2021).

Our proposed Patherea-P2P approach (Section 3) builds upon P2PNet (Song et al., 2021) and introduces a Hybrid Hungarian Matching to increase the amount of positive supervision in comparison with the vanilla one-to-one matching utilized in P2PNet, as well as DETR-based approaches. Implicitly, this also incorporates contextual information. We also design our architecture around a standard visual backbone with a lightweight head, in comparison with object detection specific DETR-based architectures, which limit the use of large pre-trained foundational models.

## 2.2. Datasets

Supervised deep-learning approaches require lots of labeled training data. Acquiring labeled data in the medical imaging domain is particularly challenging,

as the samples need to be labeled by domain experts, which represents the main difference in comparison with natural images. Providing fine-grained annotations (e.g., point annotations, bounding boxes, segmentation masks) represents an even greater challenge due to the time-consuming annotation process. Larger datasets in digital pathology are thus mostly focused on patch-based classification (Litjens et al., 2018; Sirinukunwattana et al., 2017; Kather et al., 2018; Bulten et al., 2022), where particular (larger) tissue regions are delineated with polygons in WSIs, with patches being extracted and labeled based on the annotated source polygon region.

Cell (nuclei) detection and classification requires much more fine-grained labels. A selection of the most prominent datasets is presented in Table 1.

Table 1: Characteristics of different cell detection and classification datasets. Cell segmentation datasets (\*) can also be utilized. Datasets are ordered by their publication date. The WSI column indicates whether the dataset was acquired using a digital slide scanner. The manual column specifies whether the dataset was fully annotated manually.

	Stain	Organs	Magn.	Cells	Classes	WSI	Manual
BM	H&E	1	20x	4,205	1	✓	✓
CRC	H&E	1	20x	22,444	4	✓	✓
CoNSeP*	H&E	1	40x	24,319	4	✓	✓
PanNuke*	H&E	19	20/40x	189,744	5	✓	✗
BCData	Ki-67	1	40x	181,074	2	✗	✓
Lizard*	H&E	1	20x	495,179	6	✓	✗
BRCA-M2C	H&E	1	20x	30,638	3	✓	✓
OCELOT	H&E	6	40x	114,700	2	✓	✓
Patherea ( <b>ours</b> )	Ki-67	7	40x	202,887	5	✓	✓

First point-based datasets (e.g., BM (Kainz et al., 2015), CRC (Sirinukunwattana et al., 2016)) were manually labeled single-organ datasets with a limited number of labeled cell nuclei and cell types. Some of the datasets are labeled at 20x objective magnification, which significantly reduces the level of morphology present in cellular structures, which can hinder effective cell detection and classification. Access to large-scale 40x objective magnification samples is limited, as hospitals mostly archive 20x samples, due to storage constraints. Cell segmentation and detection datasets were also introduced (e.g., CoNSeP (Graham et al., 2019), PanNuke (Gamper et al., 2019), Lizard (Graham et al., 2021)) which usually also have point-based annotations, or can be manually computed as centroids of the segmen-

tation masks.

Cell segmentation datasets (Gamper et al., 2019; Graham et al., 2021) were mostly labeled in a semi-automatic fashion, by manually labeling a small fraction of the samples, training the model, applying the model on new samples, followed by a manual step of (frequently limited) expert-level correction. The Lizard dataset (Graham et al., 2021) represents the largest dataset with close to 500k labeled nuclei. A slightly extended version of the Lizard dataset was also part of the recent CoNIC nuclear detection, segmentation, classification and counting challenge (Graham et al., 2024).

BCData (Huang et al., 2020), BRCA-M2C (Abousamra et al., 2021) and OCELOT (Ryu et al., 2023) are more recent datasets that were specifically designed for the task of point-based cell detection and classification tasks. BCData (Huang et al., 2020) represents a similar task to our proposed Patherea-Breast (Section 4.2) dataset, and the only dataset that uses stains beyond the standard H&E, but was collected using a standard microscope, with an attached camera. OCELOT (Ryu et al., 2023) additionally provides a larger field-of-view pair of cell and tissue annotations.

Our proposed Patherea dataset to the best of our knowledge represents the largest, fully-manually-labeled point-based cell detection and classification dataset acquired at 40x objective magnification. In comparison with related work (Table 1), we acquire the dataset in a way that mimics the traditional clinical workflow with a microscope, with expert pathologists interactively using the full WSIs at different magnifications to label the regions and cellular structures of interest.

### 2.3. Pathology Foundational Models

Transfer learning from a supervised pre-trained ImageNet (Deng et al., 2009; Yosinski et al., 2014) backbone has been a widely established approach in general computer vision. Recently, transfer-learning from a self-supervised pre-training showed promising results in various downstream tasks (Ericsson et al., 2021; Goldblum et al., 2024). This is even more evident in the medical imaging domain (Azizi et al., 2021), where large supervised pre-trained models are not available for a specific domain. The benefits of using self-supervised pre-training for fine-grained downstream tasks (e.g., detection, segmentation) have been less evident (Goldblum et al., 2024), especially with earlier, contrastive-based approaches (Chen et al., 2020; Caron et al., 2021). Lately, masked-image-modeling has been proposed (Xie et al., 2022; He et al., 2022; Oquab et al., 2024; Tian et al., 2023), which pre-text task is much more suitable for fine-grained tasks.

Similar to the general computer vision domain, pathology foundational models have been recently proposed (Filiot et al., 2023; Chen et al., 2024; Vorontsov et al., 2023; Dippel et al., 2024; Xu et al., 2024; Nechaev et al., 2024) that utilize vast amounts of digitized pathology data from various organs, stains and instruments. Most of the models utilize the standard H&E data, which is available in abundance. Recent foundational models (Dippel et al., 2024; Nechaev et al., 2024) have also incorporated different stains. Most of the models are trained on proprietary training data and are not publicly available. They are predominately evaluated on various downstream clinical tasks, where a significant boost is observed in comparison with ImageNet pre-trained models (Campanella et al., 2024). We utilize a recently provided open-source Hibou pathology foundational model (Nechaev et al., 2024), based on the ViT-B backbone and apply it to the task of point-based cell detection and classification. This presents a novel application of an existing foundational model to the specific downstream task of point-based cell detection and classification.

### 3. Methods

The proposed Patherea-P2P architecture is presented in Figure 1. The overall architecture was inspired by the crowd counting and localization Point-to-Point Network (P2PNet) (Song et al., 2021), which was further extended with a novel Hybrid Hungarian-based regression loss, classification capability and modern building blocks that enable the use of self-supervised approaches to train or use existing foundational models tailored for digital pathology. The used notation mostly follows (Song et al., 2021).

#### 3.1. P2P Network

Patherea-P2P method training input represents a (histology tissue) patch with a set of  $\mathcal{P} = \{p_i\}$  point-based annotations  $p_i = (x_i, y_i, t_i), i \in \{1, \dots, N\}, t \in \{1, \dots, T\}$ , which represents a cell center location  $(x_i, y_i)$  and a cell type  $(t_i)$  for a particular cell  $i$  - among  $N$  labeled cells and  $T$  cell types in a given patch (Figure 1, left, green dots). The trained model similarly predicts a set of points  $\hat{\mathcal{P}} = \{\hat{p}_j\}$  in a given patch  $\hat{p}_j = (\hat{x}_j, \hat{y}_j, c_j^{t \in T}), j \in \{1, \dots, M\}$ , based on the  $M$  proposal candidates (Figure 1, top-right, red dots), with an additional confidence score  $c_j^{t \in T}$  for each of the  $T$  possible cell types, which we threshold to produce a final set of predictions (Figure 1, bottom-right, red dots). Predicted points  $\hat{p}_j$  should be as close as possible to ground-truth cell locations and of the same type  $t_i$ , while maximizing a confidence score  $c_j$ , for the task of cell localization. Similarly, the

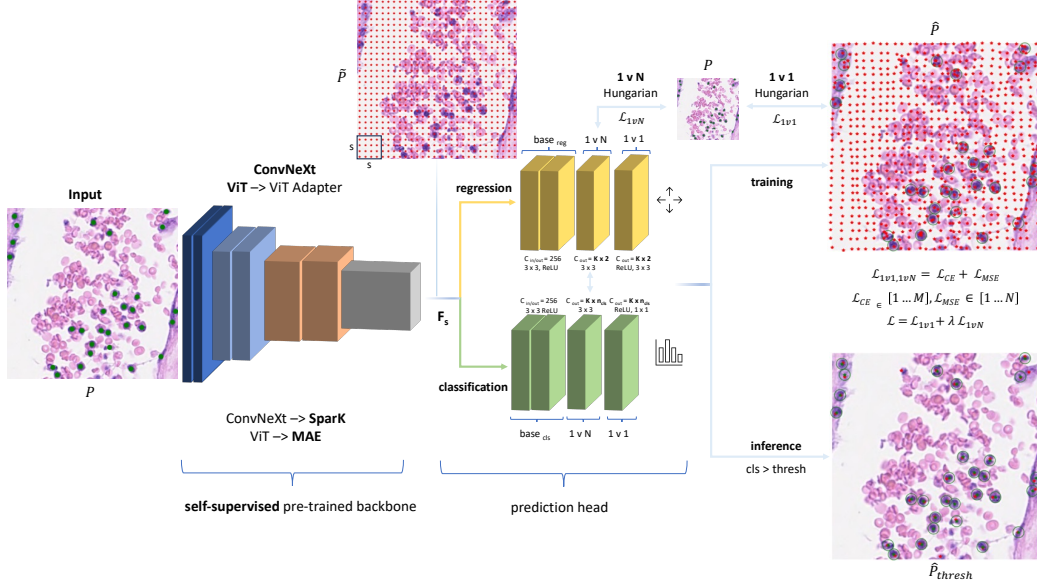


Figure 1: The proposed Patherea-P2P architecture. The green dots (●) and circles (○) represent the ground-truth annotations. Anchors (●) are initialized in a regular grid and get moved around using the regression loss (yellow head) and classified using the classification head (green).

overall number of predicted number of cells ( $\hat{N} = |c_j^{t \in T} > c_{thresh}^{t \in T}|$ ) should be as close as possible to the actual number of cells  $N$  in a given patch, for the task of cell counting. Patherea-P2P combines and optimizes both tasks at the same time, while taking into account individual cell types.

The overall architecture consists of a backbone, which encodes an image patch to the embedding  $\mathcal{F}_s$ , where  $s$  represents the downsampling stride (each positional embedding in  $\mathcal{F}_s$  represents a  $s \times s$  receptive field in the input patch). The lightweight regression head  $\mathcal{H}_{reg}$  and classification head  $\mathcal{H}_{cls}$  are attached to the backbone, which are executed in parallel. We start by a set of proposal candidate points  $\tilde{\mathcal{P}}$  (Figure 1, top, red dots), which are initialized in a regular grid along the input patch. This is achieved by initializing  $K$  proposal candidates for each receptive field of size  $s \times s$  in a  $H_f \times W_f$  sized embedding  $\mathcal{F}_s$  ( $M = H_f * W_f * K$ ). Regression head  $\mathcal{H}_{reg}$  then predicts the offsets  $\Delta_{x,y}^{k \in K}$  for each proposal  $k \in K$ . Similarly, classification head  $\mathcal{H}_{cls}$  predicts cell class for each of the  $K$  proposal candidates.

For every ground truth target from  $\mathcal{P}$ , we need to assign a proposal from a set of predicted points  $\tilde{\mathcal{P}}$ , using a one-to-one matching strategy. Point proposals

are dynamically updated during training and there is no guarantee that the same point proposal will always be matched to the same ground truth proposal, especially in the early stages of training, where proposals compete with each other. But crucially, an optimal one-to-one matching must be found, where there is only one proposal candidate for each ground truth target. The matching process can be described with  $\Omega(\mathcal{P}, \hat{\mathcal{P}}, \mathcal{D})$ , where  $\mathcal{D}$  represents a pair-wise matching cost matrix  $N \times M$ , that needs to be optimized to produce matchings that minimize the sum of individual matching pair-wise costs (1):

$$\mathcal{D}(\mathcal{P}, \hat{\mathcal{P}}) = (\tau \|p_i - \hat{p}_j\|_2 - c_j^{t_i}), \quad (1)$$

where  $\|\cdot\|_2$  denotes the  $l_2$  distance between the matched ground truth cell location  $p_i$  and matched predicted cell location  $\hat{p}_j$ . The predicted confidence score  $c_j^{t_i}$  for the ground truth cell type  $t_i$  is utilized to resolve potential conflicts where multiple proposals  $p_j$  are of the same distance to the ground truth  $p_i$ . The confidence term also encourages the positive matches to have a higher confidence score.  $\tau$  denotes a weight term to balance the pixel distance term. The Hungarian algorithm is used for  $\Omega$  to solve the assignment problem.

Let  $\xi = \Omega(\mathcal{P}, \hat{\mathcal{P}}, \mathcal{D})$  denote the optimal permutation  $\{1, \dots, M\}$ , such that  $\hat{\mathcal{P}}_{pos} = \hat{p}_{\xi(i)}, i \in \{1, \dots, N\}$  represents the matched proposal candidate for ground truth  $p_i$ , while  $\hat{\mathcal{P}}_{neg} = \hat{p}_{\xi(i)}, i \in \{N + 1, \dots, M\}$  represents unmatched proposal candidates that are treated as background. The classification loss can thus be derived as following (2):

$$\mathcal{L}_{cls} = -\frac{1}{M} \left\{ \sum_{i=1}^M \lambda_t t_i \log c_{\xi(i)}^{t_i \in T} \right\}, \quad (2)$$

where  $\lambda_t$  denotes a cell type class weight for  $T \in \{bg, t_1, \dots, t_{|T|}\}$  and  $t_i$  denotes the ground truth cell type for the matching target  $p_i$  and  $|T|$  the number of all possible cell type classes. An additional background class  $bg$  is introduced for  $\hat{\mathcal{P}}_{neg}$ .

Regression head  $\mathcal{H}_{reg}$  is optimized using only matched targets  $\hat{\mathcal{P}}_{pos}$  using the Euclidean loss:

$$\mathcal{L}_{reg} = \frac{1}{N} \sum_{i=1}^N \|p_i - \hat{p}_{\xi(i)}\|_2^2 \quad (3)$$

The combined loss is (4):

$$\mathcal{L}_{1v1} = \mathcal{L}_{cls} + \lambda_{reg} \mathcal{L}_{reg} \quad (4)$$

where  $\lambda_{reg}$  denotes the weight to balance the regression loss.

### 3.2. Hybrid Hungarian Matching

With the P2P framework presented in Section 3.1, only one proposal candidate is selected per ground truth target (one-to-one matching). Selected targets are supervised both, with the classification loss  $\mathcal{L}_{cls}$  (2) and regression loss  $\mathcal{L}_{reg}$  (3). Unmatched proposal candidates are only supervised with the classification loss. Given that  $M > N$ , often  $M \gg N$ , there is a lack of positive supervision, especially for the regression loss. Additionally, in the earlier phases of the training, different proposal candidates are often selected and partially optimized, resulting in many candidates being localized and classified "correctly", however, in the later stages of training, these candidates are treated as negative examples. This is depicted in Figure 1 (top-right), where multiple proposal candidates are positioned on the cell (or even within the more restrictive ground-truth radius). The one-to-one matching described in 3.1 selects only the closest one by distance and highest confidence when in practice, multiple candidates can be equally good. This mixed supervision - "good" candidates are being treated as background - results in sub-optimal optimization and reduced performance.

We propose a hybrid matching scheme, that first performs one-to-many matching, followed by the standard one-to-one matching, as depicted in Figure 1. The prediction head outputs are used to perform the one-to-many matching, while being further refined in the last layer with the standard one-to-one matching. This ensures more supervision signal from one-to-many optimization, while still enabling end-to-end point-based object detection, without the need for post-processing (e.g., non-maxima suppression).

We implement this by relaxing the Hungarian algorithm to enable multiple candidates to match the ground truth targets. This is achieved by replicating ground truth targets in a cost matrix  $\mathcal{D}$  by a factor of  $\beta$ , where  $\beta$  represents the number of candidate proposals per ground truth target. This allows the Hungarian algorithm to match multiple proposal candidates per ground truth target, with  $\beta = 1$  representing the standard P2P framework presented in 3.1. This results in a new cost matrix  $\hat{\mathcal{D}}$  with dimensions  $(N \times \beta) \times M$ . The losses (2) and (3) are computed in the same manner, the only difference being more matched positive samples ( $N = \beta \times N$ ), resulting in  $\mathcal{L}_{1vN}$ . The combined loss is then:

$$\mathcal{L} = \mathcal{L}_{1v1} + \lambda_{one2many} \mathcal{L}_{1vN}, \quad (5)$$

where  $\lambda_{one2many}$  denotes the balancing weight between the one-to-one and one-to-many matchings.

### 3.3. Foundational Backbone

The proposed Patherea-P2P method removes the need for any intermediate representations on the input side, as well as any post-processing, thus making it fully end-to-end. Additionally, we design the architecture in a simplified manner, reducing the need for complex task-specific building blocks, beyond the lightweight heads. Most of the existing work (Huang et al., 2023b,a; Pina et al., 2024) base their architecture on DETR-based frameworks. Vision, or even tasks-specific (e.g., object detection) approaches are usually more complex, but have usually achieved better performance due to the inherent inductive bias present in the architecture. We design the architecture around general-purpose architectures like ConvNext (Liu et al., 2022) and ViT (Dosovitskiy et al., 2021), which directly support (multi-modal) pre-training in a self-supervised manner. We utilized ConvNext and ViT backbones, together with Feature Pyramid Networks (FPN) (Lin et al., 2017), which enables to use of higher-resolution features, beneficial for dense prediction tasks. For ViT, we additionally utilized ViT-Adapter (Chen et al., 2023), which allows plain ViT to achieve comparable performance to vision-specific transformers.

Masked image modelling can be used to train foundational models from scratch using MAE (He et al., 2022) for ViT or SparK (Tian et al., 2023) for ConvNext. Alternatively, existing, open-source pathology foundational models (Nechaev et al., 2024) can be used, which are most often only available for ViTs.

## 4. Patherea Dataset

### 4.1. Background

We present, to the best of our knowledge, the largest public dataset for cell detection and classification on immunohistochemistry samples for the clinical problem of Ki-67 proliferation index estimation in neuroendocrine tumors (NETs) at different locations (small and large intestine, appendix, larynx, pharynx, lungs) and breast cancer. Both cancer types were selected due to well-standardized usage of Ki-67 as a classification/grading parameter by World Health Organization and other relevant standardization bodies and comparative studies (Polley et al., 2013; Reid et al., 2015; Dowsett et al., 2011; Nielsen et al., 2021). There is also a significant lack of publicly available datasets with immunohistochemistry stainings, with vast majority of the public pathology datasets being the standard H&E staining.

Ki-67 proliferation index is calculated as a proportion of positive tumor cells against the negative tumor cells. For example, International Ki-67 in Breast Cancer Working Group (Dowsett et al., 2011) recommends counting at least 1000 tumor



cells in at least three high-power (x40 objective) fields. In practice, "eye-balling" is often used (Reid et al., 2015), which basically means estimating the percentage of Ki-67 positive tumor cells by "scanning" the entire slide at intermediate power (x10 objective), without actually counting the individual cells. This results in a low inter-observer agreement (Reid et al., 2015) in comparison with manual counting. The development of AI-based approaches holds the potential to enable scoring Ki-67 at a fraction of the time needed, even in comparison with eye-balling, while reaching the inter-observer agreement of the manual counting. The focus of this work is to develop an efficient approach for cell detection and classification and compare its performance against the ground truth data from pathologists. Clinical relevance of an AI-assisted Ki-67 proliferation scoring and comparison against the pathologists will be the scope of the subsequent publications.

#### 4.2. Dataset

We collected 42 samples of NETs at the Institute of Pathology, Faculty of Medicine, University of Ljubljana and 29 samples of breast cancer at the Institute of Oncology Ljubljana. All the samples were scanned at x40 objective using Hamamatsu NanoZoomer S360. Ethical approvals were obtained from the National Medical Ethics Committee of the Republic of Slovenia for NETs (No. 0120-357/2023/23), as well as breast cancer (No. 0120-147/2024-2711-3).

In comparison with the related work (Sirinukunwattana et al., 2016; Huang et al., 2020; Graham et al., 2021; Abousamra et al., 2021; Ryu et al., 2023), we directly used WSIs for labeling and not the selected extracted patches, such that we directly mimicked the actual clinical workflow, if it were to be digitized. We deployed the Digital Slide Archive platform (Gutman et al., 2017) in a cloud environment for the management of WSIs, as well as for the labeling. The selected slides were labeled by 4 pathologists and each of the pathologists had access to the platform and labeled the slides through a web browser. The pathologists were free to select the regions to be labeled, which were marked with a polygon, with all of the cells and their types labeled - as depicted in Figure 2. The pathologists had access to the WSI and were able to freely navigate across the slide and use different magnifications to label the cells. Five different classes of cells were labeled: positive and negative tumor cells, cells that show proliferation, but are not tumor cells - others positive, others negative, as well as normal healthy cells. The selected samples represent biopsies of the cancer tissue, resulting in a low occurrence of healthy cells. As described in Section 4.1, the ratio between positive and negative tumor cells is important to derive the Ki-67 proliferation index.

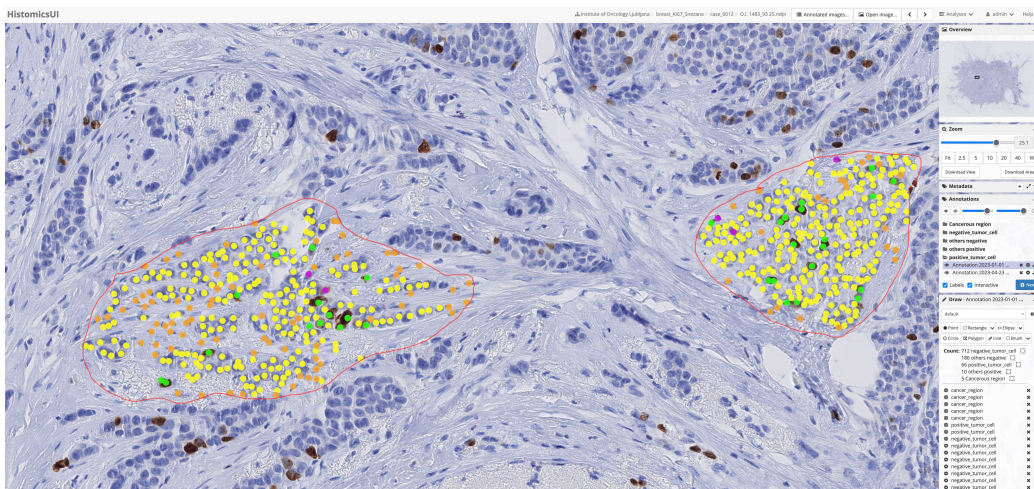


Figure 2: An example of the labeled WSI from the Digital Slide Archive. The pathologists selected the polygon regions (red) and labeled all the cells and their types using point-based annotations. Different colors represent different cell types, as defined in Table 2.

We divided the samples across three different sets - LNET, GNET and Breast. LNET part of the dataset represents the NET samples from larynx, pharynx and lungs. GNET part of the dataset represents the NET samples from the gastrointestinal tract. The Breast part of the dataset represents breast cancer samples. Each sample was labeled by one senior pathologist. Publicly available datasets are usually labeled by junior pathologists or students and later verified by a senior pathologist. In comparison, all of our samples were labeled by senior pathologists with an average of around 25 years of working experience in clinical practice. Some large-scale datasets (Graham et al., 2021) are labeled in a semi-automatic fashion, where cell centers are first proposed by an automatic (e.g. AI) approach, which are then verified by a pathologist. In comparison, we labeled all of our samples completely manually, thus producing high-quality annotations.

Different parts of the Patherea dataset, the number of samples and the number of different cells labeled are summarized in Table 2. In total, more than 200k cells of different types were labelled across 100 samples, which, to the best of our knowledge represents the largest publicly available fully-manually labeled cell detection and classification dataset.

Nevertheless, there is some inherent bias with assigning cell types, including with senior pathologists. This is especially evident with border cases, such

Table 2: Statistics of the Patherea dataset. Different colors represent the colors used to represent different cell types across all the Figures in this manuscript. Breast-P1 and Breast-P2 represents the same dataset and ROIs that were labeled by two different pathologists.

	$N_{samples}$	$N_{pos}^{\bullet}$	$N_{neg}^{\bullet}$	$N_{othr\_pos}^{\bullet}$	$N_{othr\_neg}^{\bullet}$	$N_{norm}^{\bullet}$	$\Sigma$
LNET	20	25,118	35,288	660	10,334	80	71,480
GNET	22	6,458	43,606	761	10,762	-	61,587
Breast-P1	29	9,665	17,187	908	8,913	-	36,673
Breast-P2	29	8,813	18,583	274	5,477	-	33,147
$\Sigma$	100	50,054	114,664	2,603	35,486	80	<b>202,887</b>

as other positive and negative cells. We have thus labeled the Breast part of the Patherea dataset by two pathologists. The same regions that were selected by the first pathologist were given to the second pathologist, which labeled all of the cells in the regions that were selected by the first pathologist. This is depicted in Table 2 by Breast-P1 and Breast-P2.

Annotated WSIs were then patched into patches of  $224 \times 224$  and split into 3 folds, that were used to train and evaluate different models in Section 6. The dataset, including the raw WSIs and the patched folds, will be made publicly available.

## 5. Evaluation Protocol

As described in Section 4, we only obtain point-based annotations and subsequently define a ground truth region as a circular region with radius  $r$  centered at a cell center labeled by a pathologist. We can then match all the detected cell centroids with the corresponding pathologist annotations. We can then compute a per-class F1 score based on true-positives (TP), false-positives (FP) and false-negatives (FN), as depicted in Figure 3 - left and equation (6).

$$F1_{cls} = \frac{TP}{TP + \frac{1}{2}(FP + FN)} \quad (6)$$

The Hungarian algorithm is used by most of the established public datasets and benchmarks (Xie et al., 2018; Graham et al., 2019; Huang et al., 2023b,a) to perform the one-to-one matching between the detections and labeled ground

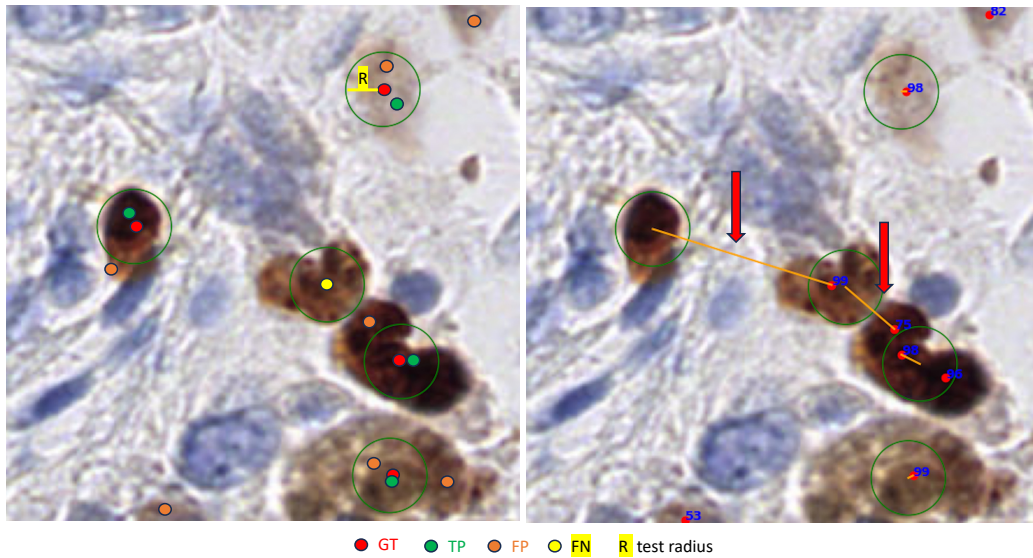


Figure 3: Left: Visual representation of F1 metric computation based on the visual detections and circular ground truth regions. Right: Depiction of wrongly assigned matches when performing Hungarian one-to-one matching directly on the distance matrix. Numbers represent the predicted confidence.

truth data. Some of the established benchmarks (Graham et al., 2019) have performed the Hungarian matching in a flawed manner<sup>3</sup>, which does not report the correct F1 scoring. Such flawed scoring is then used by the following work (Huang et al., 2023b,a), which prevents a fair comparison against different approaches and datasets, if not the same benchmarking code is used - which would still result in an underestimated F1 score. The problem arises due to the global cost optimization nature of the Hungarian algorithm, if directly a distance matrix is used to do the assignments. This is depicted in Figure 3 - right, that depicts the flawed nature of assignments.

Due to the global objective optimization, a distant detection, correctly detected for one of the ground truth cells is assigned to another cell, that has no close detection (e.g., Figure 3, left arrow). A detection, close-by, but outside of the ground truth circular region is assigned to the first ground truth location (e.g., Figure 3, right arrow). After the Hungarian matching, filtering based on the ground truth

<sup>3</sup>[https://github.com/vqdang/hover\\_net/blob/master/metrics/stats\\_utils.py#L393](https://github.com/vqdang/hover_net/blob/master/metrics/stats_utils.py#L393)

radius  $r$  is used. Due to the wrongly predicted point being matched to the first cell, an additional false-negative is produced, despite the first cell being correctly detected in the first place. This is the result of the global nature of the Hungarian optimization objective.

The solution, correctly implemented in the broader domain of crowd counting and localization (Wang et al., 2020) is to perform the Hungarian algorithm on a Boolean matrix, obtained by thresholding the distance matrix based on the ground truth radius  $r$ . This ensures that the matching is correct, with the only limitation being that there is no guarantee that if multiple detections are present in a circular region, the closest one to the center will be selected. This does not influence the correctness of the reported F1 score.

The alternative greedy approach of iterating across all the predicted points and ground truth data is used by some of the related work (Abousamra et al., 2021), which is also often flawed<sup>4</sup>, by allowing multiple predictions within the ground truth radius count as true-positives (one-to-many matching), which overestimates the F1 score.

The benchmarking code will be released alongside the dataset presented in Section 4 that addresses the above-mentioned problems to enable a reproducible and robust comparison across different datasets and approaches.

## 6. Experiments

In this section we report results on two established public datasets for point-based cell detection and classification - Lizard (Graham et al., 2021) and BRCA-M2C (Abousamra et al., 2021) in Section 6.2. Additionally, we also report results on BCData (Huang et al., 2020) in Appendix A.3. We report results on our newly introduced Patherea dataset in Section 6.3. We compare the proposed Patherea-P2P method introduced in Section 3 against the recent DETR-based approaches ACFormer (Huang et al., 2023b) and PGT (Huang et al., 2023a), as well as against more traditional approaches with an intermediate representation(s). For the traditional approaches, we compared against MCSpatNet (Abousamra et al., 2021), which additionally utilizes spatial context information and against our implementation of the approach from (Xie et al., 2018) - named Patherea-FCRN, which was modernized with ResNet-34 backbone and added support for cell classification, mostly following (Lee et al., 2021). We used the official code for ACFormer,

---

<sup>4</sup>[https://github.com/TopoXLab/MCSpatNet/blob/main/03\\_eval\\_localization\\_fscore.py#L17](https://github.com/TopoXLab/MCSpatNet/blob/main/03_eval_localization_fscore.py#L17)

PGT and MCSpatNet, including their publicly available pre-trained weights, when available for Lizard (Appendix A.1) or BRCA-M2C (Appendix A.2) datasets. We will publicly release the modernized re-implementation of FCRN (Xie et al., 2018) as no official code was released with the paper. F1 scores for Lizard, BRCA-M2C and Patherea datasets have been reported using the evaluation protocol described in Section 5.

### 6.1. Implementation Details

Patherea-P2P and FCRN (Xie et al., 2018) methods were implemented in PyTorch, while the official code and parameters were used to reproduce MCSpatNet (Abousamra et al., 2021), ACFormer (Huang et al., 2023b) and PGT methods (Huang et al., 2023a) on selected datasets. Patherea-P2P proposal candidates were initialized with  $K = [2, 2]$  and a Feature Pyramid Network (FPN) (Lin et al., 2017) was used for ConvNext (Liu et al., 2022) and ViT (Dosovitskiy et al., 2021) backbones with number of features set to 256 for ConvNext-B and 768 for ViT-B. Only higher-resolution features at level 2 of the FPN were used as an input to  $\mathcal{H}_{reg}$  and  $\mathcal{H}_{cls}$ . Lightweight regression and classification heads were attached with two ResNet blocks (He et al., 2016) and two  $3 \times 3$  convolutions for one-to-one and one-to-many hybrid Hungarian matching.

We use  $\tau = 0.05$  as a weight term for the pixel distance in the Hungarian matching. In a hybrid Hungarian matching setup,  $\beta = 2$  was used for public datasets reported in Section 6.2, while  $\beta = 6$  was used for the Patherea dataset, due to the increased resolution of the dataset. The influence of parameter  $\beta$  is investigated in Section 6.5. A class weighting term  $\lambda_t$  in  $\mathcal{L}_{cls}$  was set to 0.5 for the background class and 10 for all the foreground classes  $t \in T$ . Regression loss weight in  $\mathcal{L}_{1v1}$  and  $\mathcal{L}_{1vN}$  was set to  $2e - 3$ , while  $\lambda_{one2many}$  in a combined loss  $\mathcal{L}$  was set to 0.5. Threshold on confidence  $c_{thresh}^{t \in T}$  in inference was set to 0.9 for all classes  $t \in T$  for Lizard (Graham et al., 2021) and BRCA-M2C (Abousamra et al., 2021) datasets, while 0.5 was used for Patherea dataset.

ImageNet pre-trained weights were used to initialize the backbone, except when pathology foundational model (Nechaev et al., 2024) was specifically mentioned. Both, Patherea-P2P and FCRN methods were trained for 1000 epochs on public datasets (Section 6.2), while 100 epochs were used for the Patherea dataset in Section 6.3. This is due to the much larger Patherea dataset, which makes training competing methods inefficient for larger training cycles. The batch size was set to 16 and AdamW (Loshchilov and Hutter, 2019) was used as an optimizer with a learning rate set to  $1e - 4$ , weight decay to  $2e - 3$  and cosine annealing scheduler, with a linear warm-up in all experiments.

## 6.2. Public Datasets

**Lizard:** Lizard dataset was introduced in (Graham et al., 2021) and consists out of 6 different public datasets of colon cancer, where 291 images were extracted at x20 objective magnification. The Lizard dataset was primarily developed for nuclear instance segmentation and classification, but also provided cell center locations which can be utilized to develop and evaluate point-based approaches. The dataset was mostly automatically labeled, with a HoVer-Net (Graham et al., 2019) trained on existing public data and used as an initial segmentation result. The segmentation results were later refined by a pathologists and a model was re-trained. Similarly, cell class refinement was augmented with pathologists-in-the-loop. This semi-automatic approach enabled the annotation of 495,179 cells of 6 different classes (epithelial, lymphocyte, plasma, neutrophil, eosinophil, connective).

The dataset was split into 3 folds and we followed the evaluation protocol used in ACFormer and PGT and used fold 3 for training, fold 2 for validation and fold 1 for testing. The ground truth radius  $r$  was set to 6 pixels. We report the results in Table 3.

Table 3: Results on the Lizard dataset using 5x re-training strategy. Average F1 scores are reported. Standard deviation is also reported for  $F1_{avg}$ . <sup>†</sup> represents foundational model.

	$F1_{con}$	$F1_{eos}$	$F1_{epi}$	$F1_{lym}$	$F1_{neu}$	$F1_{pla}$	$F1_{avg}$
MCSpatNet	0.659	-	0.800	0.705	-	0.437	0.434 ±0.003
ACFormer	0.723	<b>0.565</b>	<u>0.816</u>	<b>0.771</b>	0.405	<b>0.580</b>	<u>0.643</u> ±0.012
PGT	<u>0.718</u>	0.534	<b>0.833</b>	<u>0.757</u>	0.283	0.538	0.611 ±0.009
FCRN	<u>0.573</u>	0.019	0.720	0.664	0.048	0.289	0.386 ±0.014
<b>ours</b> (ViT)	0.665	0.452	0.782	0.734	0.366	0.500	0.583 ±0.007
<b>ours</b> (ViT) <sup>†</sup>	0.680	0.499	0.788	0.742	<u>0.444</u>	0.524	0.613 ±0.005
<b>ours</b> (CNN)	<b>0.730</b>	<u>0.543</u>	<u>0.816</u>	<b>0.771</b>	<b>0.448</b>	<u>0.569</u>	<b>0.646</b> ±0.007

We report the results using the 5x re-training strategy to demonstrate real-world robustness and reproducibility. We report the average of the F1 scores across the 5 training runs. The official training code and recipes were used to re-train the models, except for the MCSpatNet and our re-implementation of the FCRN method, which did not report the results on the Lizard dataset. The checkpoint was selected using the best results on the validation set. We also report results using the officially provided pre-trained weights on Lizard for ACFormer and PGT in Appendix A.1, where the improvements of our model are even more significant.

The best results are achieved using our proposed Patherea-P2P approach, using the ConvNext backbone. We hypothesize that the dataset of only 291 is too small for the ViT backbone to generalize and learn the inductive biases, despite ImageNet initialization. Another reason could be low resolution of input images, scanned at 20x objective magnification and compressed, which basically removes most of the cell morphology information. We slightly improved ViT results by using a pathology foundational model<sup>†</sup> (Section 6.5). We also noticed that density-based approaches MCSpatNet and FCRN performed significantly worse, mostly due to inability to detect eosinophil and neutrophil classes. These two classes are in low abundance (e.g., 3,604 and 4,824 labels in comparison with more than 100k for epithelial, lymphocyte and connective).

**BRCA-M2C:** This breast cancer dataset was introduced with the MCSpatNet (Abousamra et al., 2021) and consists of 120 patches belonging to 113 patients, collected from TCGA. The dataset was collected at 20x objective magnification with inflammatory (lymphocyte), epithelial and stromal cells being labeled as point-based annotations. The ground truth radius  $r = 6$  was used for evaluation. We report results in Table 4.

Table 4: Results on BRCA-M2C dataset using 5x re-training strategy. Average F1 scores are reported. Standard deviation is also reported for  $F1_{avg}$ . <sup>†</sup> represents foundational model.

	$F1_{epi}$	$F1_{lym}$	$F1_{str}$	$F1_{avg}$
MCSpatNet	0.764	0.594	0.525	0.628 ±0.009
ACFormer	0.645	0.528	0.447	0.540 ±0.084
PGT	<b>0.777</b>	<u>0.625</u>	<u>0.524</u>	0.642 ±0.014
FCRN	0.725	0.579	0.472	0.592 ±0.013
<b>ours</b> (ViT)	0.753	0.629	0.502	0.628 ±0.007
<b>ours</b> (ViT) <sup>†</sup>	0.768	<b>0.674</b>	0.509	<b>0.650</b> ±0.005
<b>ours</b> (CNN)	<u>0.772</u>	<u>0.636</u>	<b>0.525</b>	<u>0.644</u> ±0.007

We report the results using the 5x re-training strategy and report the average F1 scores across the 5 training runs. Our proposed approach again achieved the best results using the ConvNext backbone, due to the small size of the BRCA-M2C dataset. The performance of the ViT-based backbone improved when the pathology foundational model<sup>†</sup> was used for pre-training. We also report results using the official weights for ACFormer and PGT in Appendix A.2.



### 6.3. Patherea Dataset

We evaluate the proposed Patherea-P2P method on our newly proposed Patherea dataset introduced in Section 4. We split the Patherea dataset into 3 folds across different patients in a random manner and perform 3-fold cross-validation for all the approaches. The splits across the folds are released alongside the Patherea dataset. The normal cells were excluded from the analysis, as only 80 cells were labeled across all parts of the Patherea dataset. We used a fixed training schedule of 100 epochs for all the methods and report the average across the folds at 100 epochs. We report the results across different parts of the Patherea dataset - LNET in Table 5, GNET in Table 6 and Breast in Table 7.

Overall, Patherea-P2P approach outperforms all of the competing approaches by a significant margin (e.g., 4-13%) in comparison with the second best approach across different Pathera datasets. The improvement is more significant with less abundant classes of others positive and others negative classes. Interestingly, density-estimation-based approaches MCSpatNet and FCRN outperformed recently proposed DETR-based approaches.

Table 5: Results on Patherea-LNET dataset. Average F1 scores are reported for 3-fold cross-validation.

	$F1_{pos}$	$F1_{neg}$	$F1_{othr\_pos}$	$F1_{othr\_neg}$	$F1_{avg}$	$t_f/N_{gpu}$
MCSpatNet	0.790	0.734	0.190	0.446	0.540	1d18h/1
ACFormer	0.826	0.781	-	-	0.402	1d18h/4
PGT	0.789	0.758	-	-	0.387	1d19h/4
FCRN	0.787	0.750	0.245	0.467	0.562	4h/1
<b>ours (ViT)</b>	<b>0.832</b>	<b>0.790</b>	<u>0.273</u>	<b>0.572</b>	<u>0.617</u>	2.1h/1
<b>ours (CNN)</b>	<u>0.828</u>	<u>0.789</u>	<b>0.318</b>	<u>0.559</u>	<b>0.624</b>	<b>1.5h/1</b>

Patherea-P2P method based on the ViT backbone consistently outperformed the ConvNext backbone. This implies that our proposed approach effectively utilizes the additional scale of the data, in comparison with existing public datasets used in Section 6.2, where performance is largely saturated. Patherea dataset can thus serve as baseline dataset to benchmark new proposed approaches. Additionally, the others positive and others negative classes present a significant challenge due to their visual similarity with positive and negative tumor cells. We hypothesize that the performance on those two classes could be further improved with approaches that can more effectively handle imbalanced datasets.

Table 6: Results on Patherea-GNET dataset. Average F1 scores are reported for 3-fold cross-validation.

	$F1_{pos}$	$F1_{neg}$	$F1_{othr\_pos}$	$F1_{othr\_neg}$	$F1_{avg}$
MCSpatNet	0.612	0.825	0.127	0.579	0.536
ACFormer	0.584	0.827	-	-	0.353
PGT	0.598	0.825	-	-	0.356
FCRN	0.746	<u>0.842</u>	-	0.629	0.555
<b>ours (ViT)</b>	<b>0.774</b>	<b>0.852</b>	<b>0.241</b>	<b>0.658</b>	<b>0.631</b>
<b>ours (CNN)</b>	<u>0.756</u>	<u>0.842</u>	<u>0.214</u>	<u>0.649</u>	<u>0.615</u>

Table 7: Results on Patherea-Breast dataset. Average F1 scores are reported for 3-fold cross-validation for both pathologists (P1/P2).

	$F1_{pos}$	$F1_{neg}$	$F1_{othr\_pos}$	$F1_{othr\_neg}$	$F1_{avg}$
MCSpatNet	0.771/0.690	0.680/0.696	0.315/-	<u>0.606/0.511</u>	0.593/0.474
ACFormer	0.761/0.717	0.657/0.668	-/-	-/-	0.378
PGT	<u>0.794/0.770</u>	0.713/0.742	-/-	-/-	0.377/0.378
FCRN	0.785/0.768	<u>0.736/0.762</u>	<u>0.326/0.025</u>	0.586/0.533	<u>0.608/0.522</u>
<b>ours (ViT)</b>	<b>0.804/0.776</b>	<b>0.748/0.763</b>	<b>0.341/0.143</b>	<b>0.640/0.585</b>	<b>0.633/0.567</b>
<b>ours (CNN)</b>	0.752/0.714	0.698/0.722	0.319/ <b>0.169</b>	<u>0.607/0.531</u>	0.594/ <u>0.534</u>

We also report an approximate training time per-fold on LNET dataset in Table 5. Training time of our proposed Patherea-P2P method is multi-fold faster, regardless of the chosen backbone. Note that we didn’t include pre-processing time needed to create intermediate representations for MCSpatNet and FCRN. We also only report the prompt fine-tuning training time for PGT.

#### 6.4. Qualitative Results

Qualitative results for the Patherea-P2P model are presented in Figure 4. First, we notice that proposal candidates are successfully filtered down with the Hungarian one-to-one matching and confidence thresholding (0.5), such that multiple detection occur rarely. This also holds true in most of the extreme cases, where cell size is significantly larger (e.g., LNET-4, GNET-3). Cells are successfully detected in dense regions (e.g., LNET-2, GNET-2), as well as when cell morphology is less apparent (e.g., GNET-5, Breast-4). There are some multiple detections present when cells are significantly overlapped and clustered (e.g., Breast-5).

One could utilize the non-maxima suppression to further fine-tune the predictions, which would result in the introduction of the post-processing step and break the fully end-to-end learning-based paradigm.

Labeling cells directly from WSI, replicating the real-world diagnostics represents a significant challenge in comparison with directly labeling small patches. Certainly, some cells will be missed or different cut-off thresholds will be used by different pathologists to label the specific cell. We notice some detections, that were not labeled by expert pathologists (e.g., LNET-4, GNET-3). We can also notice (Breast-4) how the model fits the pathologist that was labeling the data. Breast samples represent the same samples being labeled twice by two different pathologists. We notice, that they mostly disagree in border classes of others positive and others negative.

In Figures A.5 and A.6 we present qualitative results for Lizard (Graham et al., 2021) and BRCA-M2C (Abousamra et al., 2021) datasets. We notice that resolution is significantly lower with significantly less cell morphology visible to differentiate different cell types. We notice a confident detection of well-representative classes and similarly some spurious detections in regions where no labels are present.

### 6.5. Ablation Studies

**Hybrid Hungarian Matching:** In Table 8 we evaluate the influence of the parameter  $\beta$  which is used to select the number of candidates each ground truth target is matched against for an additional one-to-many loss in Patherea-P2P, as presented in Section 3.2. We demonstrate the effectiveness of the proposed hybrid matching, with relative performance gains of up to 7% for sufficiently represented classes and up to almost 25% for less abundant classes.

Table 8: The influence of the number of matching proposal candidates in training -  $\beta$  for Patherea-LNET dataset. Reported F1 scores are averaged across the 3 folds.  $\text{positive}_{othr}$  results are reported at 50 and 100 epochs. Relative improvement  $\Delta$  is also reported against the default setup ( $\beta = 1$ ).

$\beta$	1	2	4	6	$\Delta$ [%]
positive	0.799	0.820	0.828	<b>0.832</b>	4.1
negative	0.744	0.772	0.788	<b>0.790</b>	6.2
$\text{positive}_{othr100}$	0.292	<b>0.332</b>	0.287	0.273	13.7
$\text{positive}_{othr50}$	0.268	0.311	<b>0.332</b>	0.319	23.9
$\text{negative}_{othr}$	0.534	0.563	0.567	<b>0.572</b>	7.1

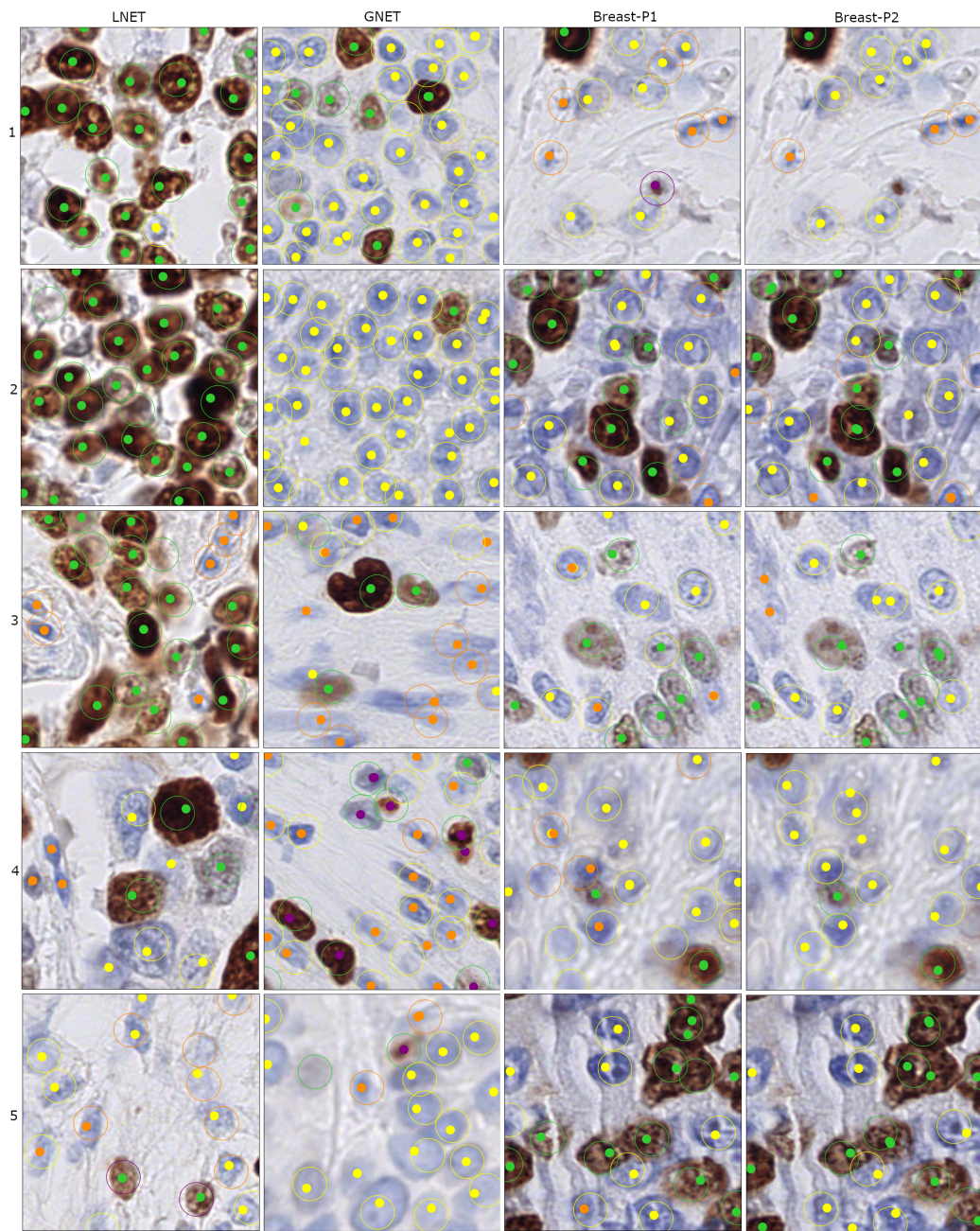


Figure 4: Patherea-P2P (ViT) qualitative results on different Patherea datasets. Example detections are displayed as filled circles, color-coded for cell type (● *pos*, ● *neg*, ● *othr\_pos*, ● *othr\_neg*). Ground-truth circular region is color coded (border) with the ground-truth cell type. Best viewed in an online version.

We notice that performance on Patherea-LNET dataset is improving with increasing  $\beta$  and starts to saturate between  $\beta = 4$  and  $\beta = 6$ . We used  $\beta = 6$  as default for Patherea dataset in Section 6.3, while  $\beta = 2$  was used for Lizard and BRCA-M2C datasets in Section 6.2 due to only x20 objective magnification used.

We also notice an overfitting against the extremely imbalanced positive<sub>othr</sub> class when evaluated at 50 and 100 epochs. The positive class starts to dominate and reduces the performance on the positive<sub>othr</sub> class with longer training.

**Foundational Model:** In Table 9 we report the average F1 performance on Lizard (Graham et al., 2021), BRCA-M2C (Abousamra et al., 2021) and Patherea-LNET datasets when using different model training strategies. For Lizard and BRCA-M2C we report the  $F1_{avg}$  across different classes with a 5x re-training strategy, directly comparable with results reported in Tables 3 and 4. Similarly to Table 5, we report  $F1_{avg}$  across the 3 folds for Patherea-LNET dataset.

Table 9: Average F1 performance when training from scratch, fine-tuning from ImageNet or using the pathology foundational model Hibou.

	Lizard	BRCA-M2C	LNET
Scratch	0.459	0.471	0.576
ImageNet	0.583	0.628	<b>0.617</b>
Hibou	<b>0.613</b>	<b>0.650</b>	<b>0.617</b>

We evaluated three different training strategies for training Patherea-P2P using the ViT backbone. i) With the *Scratch* strategy, we trained the Patherea-P2P model from scratch (backbone, ViT-Adapter, heads). ii) The 2nd approach, fine-tuning from *ImageNet* initialized ViT backbone represents the default approach used to report results in Sections 6.2 and 6.3. iii) Lastly, we utilized the recently released *Hibou* family of open-source foundational models for pathology (Nechaev et al., 2024). For *ImageNet*, we fine-tuned the whole Patherea-P2P architecture, while for *Hibou*, we only fine-tuned ViT-Adapter (Chen et al., 2023) and heads and kept the ViT backbone frozen.

We notice that training from scratch significantly reduces the performance on Lizard and BRCA-M2C datasets, while the drop on the Patherea-LNET dataset is smaller. We hypothesize that this is due to significantly smaller size of Lizard and BRCA-M2C datasets in terms of the actual number of training samples. We also notice a 3-5% improvement over ImageNet when using a foundational model on Lizard and BRCA-M2C datasets. We were able to improve upon ConvNext-based Patherea-P2P results on BRCA-M2C, reported in Table 4, when using a founda-

tional model. No improvement was observed on Patherea-LNET dataset when using a pre-trained *Hibou* foundational model. We hypothesize that this is due to the training data used in *Hibou*, where mostly H&E samples were used for training, same staining as used in Lizard and BRCA-M2C datasets. We expect to observe similar gains when foundational models start to appear, that were predominately trained on Ki-67 staining.

## 7. Conclusion

Cell detection and classification represents an essential tool to perform diagnostics in various pathology workflows. Such diagnostics workflows are extremely time-consuming for pathologists, which in practice results in performing them less accurately, leading to lower interobserver concordance and reproducibility. Automatisation of such workflows requires a significant amount of labeled data, which for the task of cell detection and classification is most efficiently obtained as point-based annotations. There is also a lack of approaches that can effectively utilize such point-based annotations and can be easily deployed in clinical practice. Ideally, the models can effectively utilize pre-trained foundational models to generalize across different cell detection and classification tasks with limited training data and/or enable efficient re-training or fine-tuning on newly collected data.

In this work, we introduced a Patherea framework that directly addresses the development of AI models in a clinical setting. First, we collected the largest fully manually labeled point-based cell detection and classification dataset for a particular clinical task of Ki-67 proliferation index estimation in Neuroendocrine tumors (NETs) and breast cancer. The annotation process was designed to mimic the ideal clinical setting, where pathologists would be manually counting the cells for the estimation of the Ki-67 index, instead of the less accurate "eye-balling" technique.

Secondly, we introduced a new approach for an automated cell detection and classification that can directly utilize point-based annotations, without the need for intermediate representations. We proposed a more efficient approach for the target-candidate association that can effectively utilize multiple (good) proposal candidates for a particular cell. We reported state-of-the-art results on existing large-scale public datasets and demonstrated that the newly proposed Patherea dataset presents a significant challenge for existing approaches, while the proposed Patherea-P2P achieving significantly better results. We also demonstrated that the proposed architecture can be effectively used to utilize existing large-scale unlabeled data to pre-train large-scale foundational models and apply them to specific tasks with a limited amount of labeled data.

We hope that the release of the Pathera framework will facilitate the development of new approaches that can effectively handle imbalanced datasets and distinguish challenging cell type classes introduced with our dataset. Comparing different approaches with reliable metrics is important, and we have revised the established scoring protocols for point-based cell detection and classification and proposed a more accurate approach.

Finally, in this work, we only addressed the specific problem of point-based cell detection and classification, without addressing the actual clinical problem of Ki-67 proliferation index estimation. In our future work, we plan to apply the proposed approaches to a large cohort of Ki-67 stained samples that have slide-level Ki-67 index estimations provided by multiple pathologists and compare that against the automatically estimated Ki-67 index that was calculated based on the approach developed in this work.

## **8. Acknowledgment**

The research was partially co-financed by funds from the Slovenian Research and Innovation Agency (ARIS), allocated to the research program groups P3-0054 (Pathology and Molecular Genetics) and P2-0214 (Computer Vision).

## Appendix A. Additional Results

### Appendix A.1. Lizard

In Table A.10 we report the results on the Lizard dataset (Graham et al., 2021) by using officially provided weights to initialize the ACFormer (Huang et al., 2023b) and PGT (Huang et al., 2023a) methods, without the need for re-training. No official training weights were provided for MCSpatNet (Abousamra et al., 2021) and FCRN (Xie et al., 2018).

We notice a slight drop in performance, when using the official weights. We report the best obtained Patherea and FCRN results after 100 training runs using using different random seeds. This gives an upper bound for the Lizard dataset. This is possible due to an efficient implementation of the Patherea approaches, which on average take around 2 hours to train on the Lizard dataset, in comparison with 2 days for MCSpatNet, ACFormer and PGT.

Table A.10: Results on Lizard dataset using official pre-trained weights for PGT and ACFormer. Best out of 5 training runs is reported for MCSpatNet. Best out of 100 training runs using different random seeds is reported for FCRN and Patherea.

	$F1_{con}$	$F1_{eos}$	$F1_{epi}$	$F1_{lym}$	$F1_{neu}$	$F1_{pla}$	$F1_{avg}$
MCSpatNet	0.661	0	0.814	0.712	0	0.442	0.438
ACFormer	<u>0.714</u>	0.506	<u>0.819</u>	0.740	0.330	<u>0.561</u>	0.612
PGT	0.712	<u>0.536</u>	0.810	<u>0.742</u>	<u>0.395</u>	0.515	<u>0.618</u>
FCRN	0.594	0.017	0.733	0.676	0.055	0.309	0.397
<b>ours (CNN)</b>	<b>0.722</b>	<b>0.570</b>	<b>0.815</b>	<b>0.780</b>	<b>0.445</b>	<b>0.585</b>	<b>0.653</b>

### Appendix A.2. BRCA-M2C

We notice that MCSpatNet (Abousamra et al., 2021) performs much better with the official weights in comparison with 5x re-training (reported in Table 4) using the official code and training recipes. We report the best obtained Patherea and FCRN results after 100 training runs using different random seeds. We notice that we are able to reach the official performance of the MCSpatNet with one of the random seeds, which suggests that best performing MCSpatNet weights were selected for release. Similar improvement is noticeable for ACFormer (Huang et al., 2023b).



Table A.11: Results on BRCA-M2C dataset using official pre-trained weights for MCSpatNet, PGT and ACFormer. Best out of 100 training runs using different random seeds is reported for FCRN and Patherea.

	$F1_{epi}$	$F1_{lym}$	$F1_{str}$	$F1_{avg}$
MCSpatNet	<b>0.793</b>	0.649	<b>0.548</b>	<b>0.663</b>
ACFormer	0.741	0.618	0.462	0.607
PGT	<b>0.792</b>	0.624	0.531	0.649
FCRN	0.777	0.583	0.489	0.616
<b>ours (CNN)</b>	<u>0.786</u>	<b>0.659</b>	<u>0.538</u>	<u>0.661</u>

### Appendix A.3. BCData

We report results on BCData (Huang et al., 2020) in Table A.12. We directly report F1 scores from the original publication for competing methods SC-CNN (Sirinukunwattana et al., 2016), CSRNet (Li et al., 2018) and U-CSRNet (Huang et al., 2020). The official implementation code was not released. No details (or code) were provided on F1 score calculation. FCRN re-implementation (Xie et al., 2018) and Patherea results are reported using our F1 benchmarking code (Section 5).

Table A.12: Results on BCData dataset. Best out of 100 training runs using different random seeds is reported for FCRN and Patherea.

	$F1_{epi}$	$F1_{lym}$	$F1_{avg}$
SC-CNN	0.798	0.778	0.788
CSRNet	0.829	0.814	0.822
U-CSRNet	<b>0.863</b>	<u>0.852</u>	<u>0.857</u>
FCRN	0.844	0.804	0.824
<b>ours (CNN)</b>	<u>0.862</u>	<b>0.854</b>	<b>0.858</b>

FCRN (Xie et al., 2018) implementation is very similar to U-CSRNet (Huang et al., 2020), but achieving lower performance. No implementation code or benchmarking details are available for U-CSRNet to verify the results.

### Appendix A.4. Qualitative Results

In Figures A.5 and A.6 we present qualitative results for Lizard (Graham et al., 2021) and BRCA-M2C (Abousamra et al., 2021) datasets. Lizard samples are collected from various public colorectal cancer datasets with various image size and

quality. BRCA-M2C samples are collected and labeled from TCGA BRCA (Lingle et al., 2016).

## References

- Abousamra, S., Belinsky, D., Van Arnam, J., Allard, F., Yee, E., Gupta, R., Kurc, T., Samaras, D., Saltz, J., Chen, C., 2021. Multi-class cell detection using spatial context representation, in: Proceedings of the IEEE/CVF International Conference on Computer Vision, pp. 4005–4014.
- Azizi, S., Mustafa, B., Ryan, F., Beaver, Z., Freyberg, J., Deaton, J., Loh, A., Karthikesalingam, A., Kornblith, S., Chen, T., et al., 2021. Big self-supervised models advance medical image classification, in: Proceedings of the IEEE/CVF international conference on computer vision, pp. 3478–3488.
- Bankhead, P., Loughrey, M.B., Fernández, J.A., Dombrowski, Y., McArt, D.G., Dunne, P.D., McQuaid, S., Gray, R.T., Murray, L.J., Coleman, H.G., et al., 2017. Qupath: Open source software for digital pathology image analysis. *Scientific reports* 7, 1–7.
- Bejnordi, B.E., Veta, M., Van Diest, P.J., Van Ginneken, B., Karssemeijer, N., Litjens, G., Van Der Laak, J.A., Hermsen, M., Manson, Q.F., Balkenhol, M., et al., 2017. Diagnostic assessment of deep learning algorithms for detection of lymph node metastases in women with breast cancer. *Jama* 318, 2199–2210.
- Bera, K., Schalper, K.A., Rimm, D.L., Velcheti, V., Madabhushi, A., 2019. Artificial intelligence in digital pathology—new tools for diagnosis and precision oncology. *Nature reviews Clinical oncology* 16, 703–715.
- Bulten, W., Kartasalo, K., Chen, P.H.C., Ström, P., Pinckaers, H., Nagpal, K., Cai, Y., Steiner, D.F., Van Boven, H., Vink, R., et al., 2022. Artificial intelligence for diagnosis and gleason grading of prostate cancer: the panda challenge. *Nature medicine* 28, 154–163.
- Campanella, G., Chen, S., Verma, R., Zeng, J., Stock, A., Croken, M., Veremis, B., Elmas, A., Huang, K.I., Kwan, R., et al., 2024. A clinical benchmark of public self-supervised pathology foundation models. *arXiv preprint arXiv:2407.06508*.

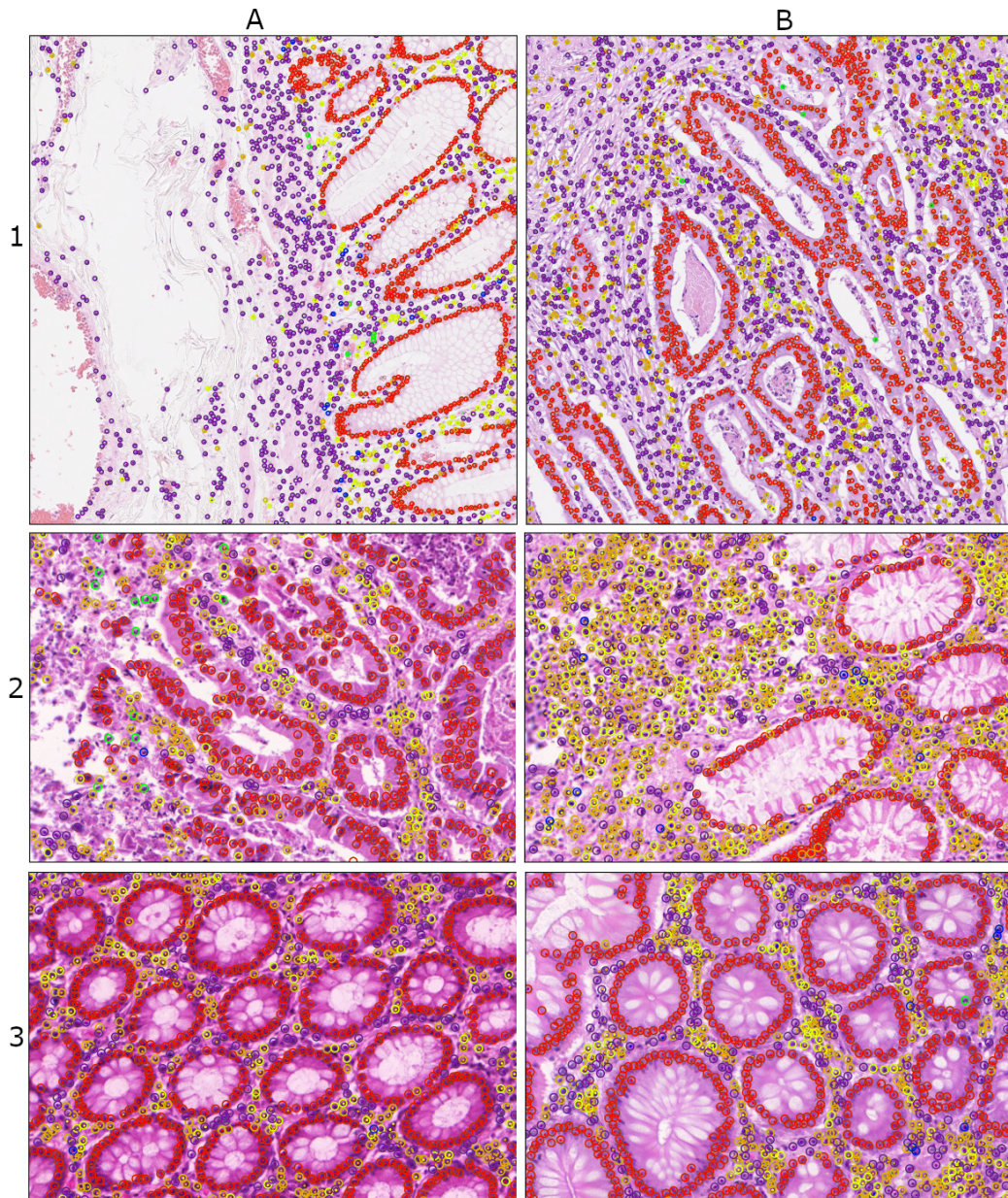


Figure A.5: Patherea-P2P (ConvNext) qualitative results on Lizard dataset. Example detections are displayed as filled circles, color-coded for cell type (● *neutrophil*, ● *epithelial*, ● *lymphocyte*, ● *plasma*, ● *eosinophil*, ● *connective*). Ground-truth circular region is color coded (border) with the ground-truth cell type. Best viewed in an online version with zoom.



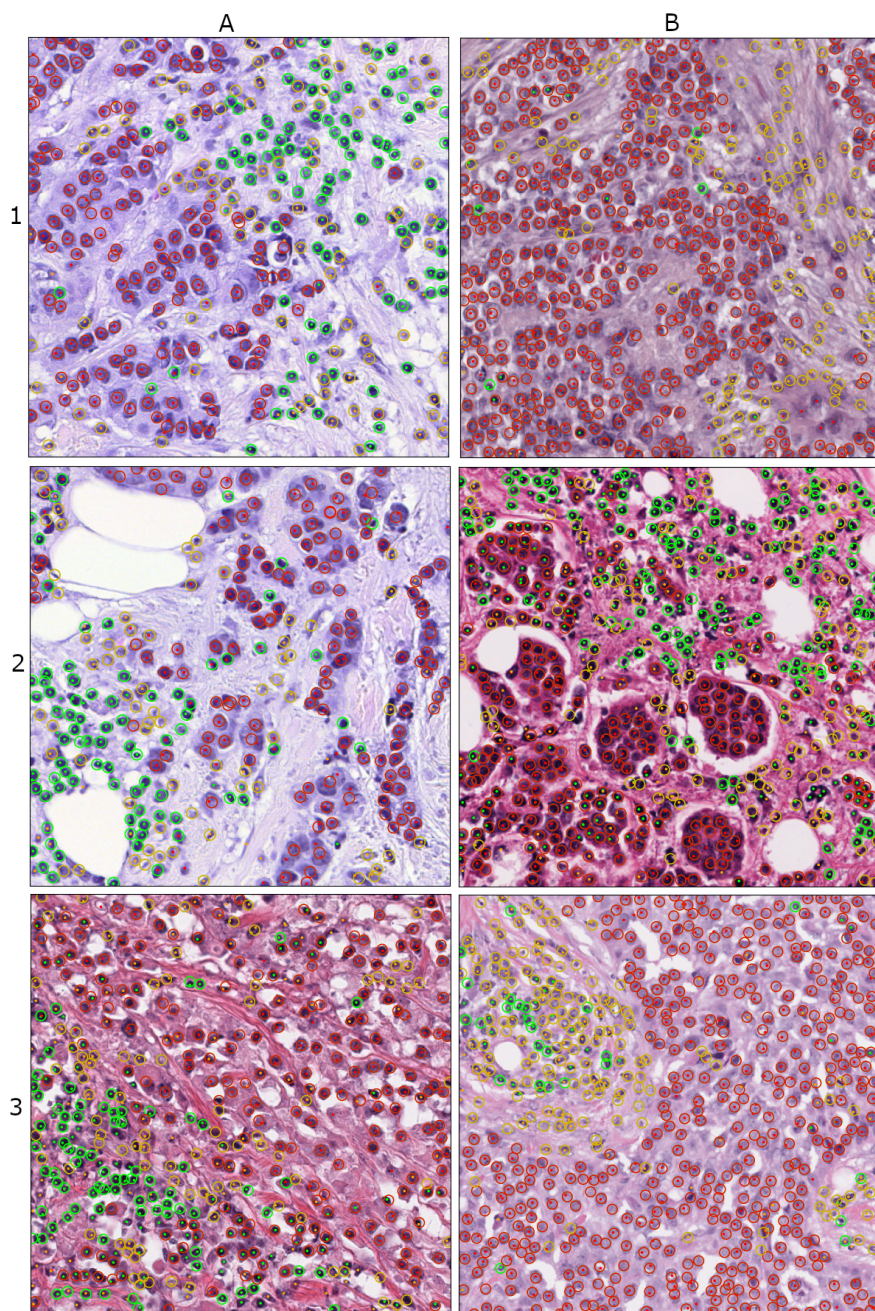


Figure A.6: Patherea-P2P (ConvNext) qualitative results on BRCA-M2C dataset. Example detections are displayed as filled circles, color-coded for cell type (● *lymphocyte*, ● *epithelial*, ● *stromal*). Ground-truth circular region is color coded (border) with the ground-truth cell type. Best viewed in an online version with zoom.

- Carion, N., Massa, F., Synnaeve, G., Usunier, N., Kirillov, A., Zagoruyko, S., 2020. End-to-end object detection with transformers, in: European conference on computer vision, Springer. pp. 213–229.
- Caron, M., Touvron, H., Misra, I., Jégou, H., Mairal, J., Bojanowski, P., Joulin, A., 2021. Emerging properties in self-supervised vision transformers, in: Proceedings of the IEEE/CVF international conference on computer vision, pp. 9650–9660.
- Chen, R.J., Ding, T., Lu, M.Y., Williamson, D.F., Jaume, G., Song, A.H., Chen, B., Zhang, A., Shao, D., Shaban, M., et al., 2024. Towards a general-purpose foundation model for computational pathology. *Nature Medicine* 30, 850–862.
- Chen, T., Kornblith, S., Norouzi, M., Hinton, G., 2020. A simple framework for contrastive learning of visual representations, in: International conference on machine learning, PMLR. pp. 1597–1607.
- Chen, Z., Duan, Y., Wang, W., He, J., Lu, T., Dai, J., Qiao, Y., 2023. Vision transformer adapter for dense predictions, in: The Eleventh International Conference on Learning Representations.
- Cui, M., Zhang, D.Y., 2021. Artificial intelligence and computational pathology. *Laboratory Investigation* 101, 412–422.
- Deng, J., Dong, W., Socher, R., Li, L.J., Li, K., Fei-Fei, L., 2009. Imagenet: A large-scale hierarchical image database, in: 2009 IEEE conference on computer vision and pattern recognition, Ieee. pp. 248–255.
- Dippel, J., Feulner, B., Winterhoff, T., Schallenberg, S., Dernbach, G., Kunft, A., Tietz, S., Jurmeister, P., Horst, D., Ruff, L., et al., 2024. RudolfV: a foundation model by pathologists for pathologists. *arXiv preprint arXiv:2401.04079* .
- Dosovitskiy, A., Beyer, L., Kolesnikov, A., Weissenborn, D., Zhai, X., Unterthiner, T., Dehghani, M., Minderer, M., Heigold, G., Gelly, S., Uszkoreit, J., Houlsby, N., 2021. An image is worth 16x16 words: Transformers for image recognition at scale, in: International Conference on Learning Representations.
- Dowsett, M., Nielsen, T.O., A’Hern, R., Bartlett, J., Coombes, R.C., Cuzick, J., Ellis, M., Henry, N.L., Hugh, J.C., Lively, T., et al., 2011. Assessment of Ki67 in breast cancer: recommendations from the International Ki67 in Breast Cancer working group. *Journal of the National cancer Institute* 103, 1656–1664.

- Ericsson, L., Gouk, H., Hospedales, T.M., 2021. How well do self-supervised models transfer?, in: Proceedings of the IEEE/CVF conference on computer vision and pattern recognition, pp. 5414–5423.
- Filiot, A., Ghermi, R., Olivier, A., Jacob, P., Fidon, L., Mac Kain, A., Saillard, C., Schiratti, J., 2023. Scaling self-supervised learning for histopathology with masked image modeling. medrxiv .
- Gamper, J., Alemi Koohbanani, N., Benet, K., Khuram, A., Rajpoot, N., 2019. Pannuke: an open pan-cancer histology dataset for nuclei instance segmentation and classification, in: Digital Pathology: 15th European Congress, ECDP 2019, Warwick, UK, April 10–13, 2019, Proceedings 15, Springer. pp. 11–19.
- Goldblum, M., Souri, H., Ni, R., Shu, M., Prabhu, V., Somepalli, G., Chattopadhyay, P., Ibrahim, M., Bardes, A., Hoffman, J., et al., 2024. Battle of the backbones: A large-scale comparison of pretrained models across computer vision tasks. Advances in Neural Information Processing Systems 36.
- Graham, S., Jahanifar, M., Azam, A., Nimir, M., Tsang, Y.W., Dodd, K., Hero, E., Sahota, H., Tank, A., Benes, K., et al., 2021. Lizard: A large-scale dataset for colonic nuclear instance segmentation and classification, in: Proceedings of the IEEE/CVF international conference on computer vision, pp. 684–693.
- Graham, S., Vu, Q.D., Jahanifar, M., Weigert, M., Schmidt, U., Zhang, W., Zhang, J., Yang, S., Xiang, J., Wang, X., et al., 2024. Conic challenge: Pushing the frontiers of nuclear detection, segmentation, classification and counting. Medical image analysis 92, 103047.
- Graham, S., Vu, Q.D., Raza, S.E.A., Azam, A., Tsang, Y.W., Kwak, J.T., Rajpoot, N., 2019. Hover-net: Simultaneous segmentation and classification of nuclei in multi-tissue histology images. Medical image analysis 58, 101563.
- Gutman, D.A., Khalilia, M., Lee, S., Nalisnik, M., Mullen, Z., Beezley, J., Chittajallu, D.R., Manthey, D., Cooper, L.A., 2017. The digital slide archive: a software platform for management, integration, and analysis of histology for cancer research. Cancer research 77, e75–e78.
- He, K., Chen, X., Xie, S., Li, Y., Dollár, P., Girshick, R., 2022. Masked autoencoders are scalable vision learners, in: Proceedings of the IEEE/CVF conference on computer vision and pattern recognition, pp. 16000–16009.

- He, K., Zhang, X., Ren, S., Sun, J., 2016. Deep residual learning for image recognition, in: Proceedings of the IEEE conference on computer vision and pattern recognition, pp. 770–778.
- Huang, J., Li, H., Sun, W., Wan, X., Li, G., 2023a. Prompt-based grouping transformer for nucleus detection and classification, in: International Conference on Medical Image Computing and Computer-Assisted Intervention, Springer. pp. 569–579.
- Huang, J., Li, H., Wan, X., Li, G., 2023b. Affine-consistent transformer for multi-class cell nuclei detection, in: Proceedings of the IEEE/CVF International Conference on Computer Vision, pp. 21384–21393.
- Huang, Z., Ding, Y., Song, G., Wang, L., Geng, R., He, H., Du, S., Liu, X., Tian, Y., Liang, Y., et al., 2020. Bcdata: A large-scale dataset and benchmark for cell detection and counting, in: Medical Image Computing and Computer Assisted Intervention–MICCAI 2020: 23rd International Conference, Lima, Peru, October 4–8, 2020, Proceedings, Part V 23, Springer. pp. 289–298.
- Kainz, P., Urschler, M., Schuster, S., Wohlhart, P., Lepetit, V., 2015. You should use regression to detect cells, in: Medical Image Computing and Computer-Assisted Intervention–MICCAI 2015: 18th International Conference, Munich, Germany, October 5-9, 2015, Proceedings, Part III 18, Springer. pp. 276–283.
- Kather, J.N., Halama, N., Marx, A., 2018. 100,000 histological images of human colorectal cancer and healthy tissue. Zenodo10 5281.
- Lee, S.M., Shaw, A., Simpson, J.L., Uminsky, D., Garratt, L.W., 2021. Differential cell counts using center-point networks achieves human-level accuracy and efficiency over segmentation. Scientific Reports 11, 16917.
- Li, Y., Zhang, X., Chen, D., 2018. Csrnet: Dilated convolutional neural networks for understanding the highly congested scenes, in: Proceedings of the IEEE conference on computer vision and pattern recognition, pp. 1091–1100.
- Lin, T.Y., Dollár, P., Girshick, R., He, K., Hariharan, B., Belongie, S., 2017. Feature pyramid networks for object detection, in: Proceedings of the IEEE conference on computer vision and pattern recognition, pp. 2117–2125.

- Lingle, W., Erickson, B., Zuley, M., Jarosz, R., Bonaccio, E., Filippini, J., Net, J., Levi, L., Morris, E., Figler, G., et al., 2016. The cancer genome atlas breast invasive carcinoma collection (tcga-brca)(version 3)[data set] the cancer imaging archive. *Cancer Imag Arch* .
- Litjens, G., Bandi, P., Ehteshami Bejnordi, B., Geessink, O., Balkenhol, M., Bult, P., Halilovic, A., Hermsen, M., Van de Loo, R., Vogels, R., et al., 2018. 1399 h&e-stained sentinel lymph node sections of breast cancer patients: the camelyon dataset. *GigaScience* 7, giy065.
- Liu, Z., Mao, H., Wu, C.Y., Feichtenhofer, C., Darrell, T., Xie, S., 2022. A convnet for the 2020s, in: *Proceedings of the IEEE/CVF conference on computer vision and pattern recognition*, pp. 11976–11986.
- Loshchilov, I., Hutter, F., 2019. Decoupled weight decay regularization, in: *International Conference on Learning Representations*.
- Mikami, Y., Ueno, T., Yoshimura, K., Tsuda, H., Kurosumi, M., Masuda, S., Horii, R., Toi, M., Sasano, H., 2013. Interobserver concordance of Ki67 labeling index in breast cancer: Japan Breast Cancer Research Group Ki67 Ring Study. *Cancer science* 104, 1539–1543.
- Mukhopadhyay, S., Feldman, M.D., Abels, E., Ashfaq, R., Beltaifa, S., Cacciabeve, N.G., Cathro, H.P., Cheng, L., Cooper, K., Dickey, G.E., et al., 2018. Whole slide imaging versus microscopy for primary diagnosis in surgical pathology: a multicenter blinded randomized noninferiority study of 1992 cases (pivotal study). *The American journal of surgical pathology* 42, 39–52.
- Nechaev, D., Pchel'nikov, A., Ivanova, E., 2024. Hibou: A family of foundational vision transformers for pathology. *arXiv preprint arXiv:2406.05074* .
- Nielsen, T.O., Leung, S.C.Y., Rimm, D.L., Dodson, A., Acs, B., Badve, S., Denkert, C., Ellis, M.J., Fineberg, S., Flowers, M., et al., 2021. Assessment of Ki67 in breast cancer: updated recommendations from the international Ki67 in breast cancer working group. *JNCI: Journal of the National Cancer Institute* 113, 808–819.
- Oquab, M., Darcet, T., Moutakanni, T., Vo, H.V., Szafraniec, M., Khalidov, V., Fernandez, P., HAZIZA, D., Massa, F., El-Nouby, A., Assran, M., Ballas, N., Galuba, W., Howes, R., Huang, P.Y., Li, S.W., Misra, I., Rabbat, M., Sharma, V.,



- Synnaeve, G., Xu, H., Jegou, H., Mairal, J., Labatut, P., Joulin, A., Bojanowski, P., 2024. DINOv2: Learning robust visual features without supervision. *Transactions on Machine Learning Research*.
- Pina, O., Dorca, E., Vilaplana, V., 2024. Cell-DETR: Efficient cell detection and classification in WSIs with transformers, in: *Medical Imaging with Deep Learning*.
- Polley, M.Y.C., Leung, S.C., McShane, L.M., Gao, D., Hugh, J.C., Mastropasqua, M.G., Viale, G., Zabaglo, L.A., Penault-Llorca, F., Bartlett, J.M., et al., 2013. An international Ki67 reproducibility study. *Journal of the National Cancer Institute* 105, 1897–1906.
- Radford, A., Kim, J.W., Hallacy, C., Ramesh, A., Goh, G., Agarwal, S., Sastry, G., Askell, A., Mishkin, P., Clark, J., et al., 2021. Learning transferable visual models from natural language supervision, in: *International conference on machine learning*, PMLR. pp. 8748–8763.
- Radford, A., Wu, J., Child, R., Luan, D., Amodei, D., Sutskever, I., et al., 2019. Language models are unsupervised multitask learners. *OpenAI blog* 1, 9.
- Reid, M.D., Bagci, P., Ohike, N., Saka, B., Seven, I.E., Dursun, N., Balci, S., Gucer, H., Jang, K.T., Tajiri, T., et al., 2015. Calculation of the Ki67 index in pancreatic neuroendocrine tumors: a comparative analysis of four counting methodologies. *Modern Pathology* 28, 686–694.
- Ryu, J., Puche, A.V., Shin, J., Park, S., Brattoli, B., Lee, J., Jung, W., Cho, S.I., Paeng, K., Ock, C.Y., et al., 2023. Ocelot: overlapped cell on tissue dataset for histopathology, in: *Proceedings of the IEEE/CVF Conference on Computer Vision and Pattern Recognition*, pp. 23902–23912.
- Sirinukunwattana, K., Pluim, J.P., Chen, H., Qi, X., Heng, P.A., Guo, Y.B., Wang, L.Y., Matuszewski, B.J., Bruni, E., Sanchez, U., et al., 2017. Gland segmentation in colon histology images: The glas challenge contest. *Medical image analysis* 35, 489–502.
- Sirinukunwattana, K., Raza, S.E.A., Tsang, Y.W., Snead, D.R., Cree, I.A., Rajpoot, N.M., 2016. Locality sensitive deep learning for detection and classification of nuclei in routine colon cancer histology images. *IEEE transactions on medical imaging* 35, 1196–1206.

- Song, Q., Wang, C., Jiang, Z., Wang, Y., Tai, Y., Wang, C., Li, J., Huang, F., Wu, Y., 2021. Rethinking counting and localization in crowds: A purely point-based framework, in: Proceedings of the IEEE/CVF International Conference on Computer Vision, pp. 3365–3374.
- Tian, K., Jiang, Y., qishuai diao, Lin, C., Wang, L., Yuan, Z., 2023. Designing BERT for convolutional networks: Sparse and hierarchical masked modeling, in: The Eleventh International Conference on Learning Representations.
- Vorontsov, E., Bozkurt, A., Casson, A., Shaikovski, G., Zelechowski, M., Liu, S., Mathieu, P., van Eck, A., Lee, D., Viret, J., et al., 2023. Virchow: a million-slide digital pathology foundation model. arXiv preprint arXiv:2309.07778 .
- Wang, Q., Gao, J., Lin, W., Li, X., 2020. Nwpu-crowd: A large-scale benchmark for crowd counting and localization. IEEE transactions on pattern analysis and machine intelligence 43, 2141–2149.
- Xie, Y., Xing, F., Kong, X., Su, H., Yang, L., 2015. Beyond classification: structured regression for robust cell detection using convolutional neural network, in: Medical Image Computing and Computer-Assisted Intervention–MICCAI 2015: 18th International Conference, Munich, Germany, October 5-9, 2015, Proceedings, Part III 18, Springer. pp. 358–365.
- Xie, Y., Xing, F., Shi, X., Kong, X., Su, H., Yang, L., 2018. Efficient and robust cell detection: A structured regression approach. Medical image analysis 44, 245–254.
- Xie, Z., Zhang, Z., Cao, Y., Lin, Y., Bao, J., Yao, Z., Dai, Q., Hu, H., 2022. Simmim: A simple framework for masked image modeling, in: Proceedings of the IEEE/CVF conference on computer vision and pattern recognition, pp. 9653–9663.
- Xing, F., Yang, L., 2016. Robust nucleus/cell detection and segmentation in digital pathology and microscopy images: a comprehensive review. IEEE reviews in biomedical engineering 9, 234–263.
- Xu, H., Usuyama, N., Bagga, J., Zhang, S., Rao, R., Naumann, T., Wong, C., Gero, Z., González, J., Gu, Y., et al., 2024. A whole-slide foundation model for digital pathology from real-world data. Nature , 1–8.

Yosinski, J., Clune, J., Bengio, Y., Lipson, H., 2014. How transferable are features in deep neural networks? *Advances in neural information processing systems* 27.